nature communications

Article

https://doi.org/10.1038/s41467-024-52686-8

Joint subarray acoustic tweezers enable controllable cell translation, rotation, and deformation

Received: 26 February 2024

Accepted: 18 September 2024

Published online: 20 October 2024

Check for updates

Liang Shen[1,2], Zhenhua Tian[2] ✉, Kaichun Yang[1], Joseph Rich[3], Jianping Xia[1], Neil Upreti[1], Jinxin Zhang[1], Chuyi Chen[1], Nanjing Hao[1], Zhichao Pei[1] & Tony Jun Huang[1] ✉

Contactless microscale tweezers are highly effective tools for manipulating, patterning, and assembling bioparticles. However, current tweezers are limited in their ability to comprehensively manipulate bioparticles, providing only partial control over the six fundamental motions (three translational and three rotational motions). This study presents a joint subarray acoustic tweezers platform that leverages acoustic radiation force and viscous torque to control the six fundamental motions of single bioparticles. This breakthrough is significant as our manipulation mechanism allows for controlling the three translational and three rotational motions of single cells, as well as enabling complex manipulation that combines controlled translational and rotational motions. Moreover, our tweezers can gradually increase the load on an acoustically trapped cell to achieve controllable cell deformation critical for characterizing cell mechanical properties. Furthermore, our platform allows for three-dimensional (3D) imaging of bioparticles without using complex confocal microscopy by rotating bioparticles with acoustic tweezers and taking images of each orientation using a standard microscope. With these capabilities, we anticipate the JSAT platform to play a pivotal role in various applications, including 3D imaging, tissue engineering, disease diagnostics, and drug testing.

Precise single-cell manipulation, encompassing translation[1,2], rotation[3], and deformation[4,5], is essential for cellular biology, biophysics, and biomedical engineering. The ability to translate living cells in a contact-free manner significantly enhances the capabilities of tissue engineering technologies to produce biomimetic tissues for numerous applications in regenerative medicine, and disease modeling[2]. Moreover, controllable rotational manipulation enables high-resolution 3D reconstruction of cells[3,6], and small organisms[7], thereby unveiling hidden details pertaining to cellular structure and organization. This ability has proven valuable in various areas, including cell profiling, disease diagnostics, and drug screening[3]. Furthermore, the ability to gradually deform a cell allows for the characterization of cell mechanical properties, particularly those sensitive to changes in cytoskeletal and nuclear components, offering a label-free method for evaluating these alterations[5]. This ability is also critical for mechanical phenotyping, cell classification, and the tracking of cellular metabolic dynamics[8–10] with wide-ranging applications in biophysics and biology[11–16].

Although various techniques have been developed to precisely manipulate cells, including optical tweezers[17–20], optoelectronic

[1]Department of Mechanical Engineering and Materials Science, Duke University, Durham, NC, USA. [2]Department of Mechanical Engineering, Virginia Polytechnical Institute and State University, Blacksburg, VA, USA. [3]Department of Biomedical Engineering, Duke University, Durham, NC, USA.
✉e-mail: tianz@vt.edu; tony.huang@duke.edu

tweezers[21], magnetic tweezers[22,23], acoustic tweezers[24–29], acoustodielectric tweezers[30], dielectrophoresis[31–33], electrorotation[3], and high-speed hydrodynamic flow[14], the ability to manipulate cells with complete control over all six fundamental motions remained a formidable challenge. Optical tweezers have gained popularity as a technique for manipulating micro/nano-particles[18]; however, they require complex equipment and precise alignment of optical components while also introducing the risk of laser-induced heating that may cause physiological damage to bioparticles. Optoelectronic tweezers offer the advantage of dynamically trapping cells with less power than traditional optical methods[21]. However, they fall short when attempting to achieve in-plane cell rotation and deformation. Moreover, their usages are limited by the requirement of high ionic concentration environments due to ionic shielding and Joule heating[21]. Magnetic tweezers are constrained by the complexity involved in embedding or attaching magnetic nanoparticles to cells, which may lead to cell damage[34]. While dielectrophoresis[33], electrorotation[3], and high-speed hydrodynamic manipulation[14,35] can accomplish cell translation, rotation, or deformation, respectively, none of these techniques possess all of the aforementioned functions. In addition, they lack the ability to achieve and control all six fundamental motions.

In recent years, acoustofluidics has emerged as a promising contact-free strategy for cell manipulation, offering the advantages of label-free operation and excellent biocompatibility[36–43]. With these features, acoustofluidic technologies have found numerous applications in bioparticle separation[44–49], exosome enrichment[50–52], and cell patterning[53–55], among others[56–62]. These applications typically leverage the acoustic radiation force that results from bioparticle-induced acoustic field changes[63–67], as well as the acoustic streaming that stems from acoustic energy dissipation in fluids[68–70]. Acoustic tweezers based on orthogonally arranged two pairs of transducers with phase and amplitude modulation capabilities enable 3D translation of single cells[2]. For rotational object manipulation, an early study by Busse and Wang presented a theoretical framework to predict the torque induced by orthogonal acoustic waves[71]. To achieve both translational and rotational manipulation of acoustically trapped objects, Marzo and Drinkwater developed holographic acoustic tweezers, leveraging an array of transducers to generate airborne acoustic waves and reshape the acoustic energy field to versatile patterns[72]. However, as this method uses airborne acoustic waves, it is limited to manipulating objects in the air[72]. In addition to translational and rotational object manipulation, bulk acoustic wave- and streaming-based approaches have been developed to deform cells[6,15,73–76]. Given the successes of previous studies, in the context of single-cell manipulation using surface acoustic waves (SAWs), no SAW device achieves the three critical cell manipulation functions: controllable translation, rotation, and deformation of cells. Moreover, few studies investigate the mechanisms to achieve complex manipulation that combines controlled translation and rotation of single cells.

This study presents an acoustic tweezer platform, termed the joint subarray acoustic tweezers (JSAT) system, which allows for controlling the six fundamental (three translational and three rotational) motions of single cells, achieving complex motions with controlled translation and rotation, and deforming an acoustically trapped cell, by leveraging SAW-induced radiation force and acoustic streaming vortex-induced shear force. By tuning the phases and amplitudes of orthogonal standing SAWs at low frequencies, the JSAT system traps cells and controls the trapped cell's three translational motions (i.e., u_x, u_y, and u_z). To control the cell's rotational motions (i.e., θ_x and θ_y), high-frequency standing SAW-induced acoustic streaming vortices are utilized to apply viscous torques on the trapped cell. Similarly, acoustic streaming vortices[77,78] induced by high-frequency traveling SAWs control the trapped cell's rotational degree-of-freedom (DoF) θ_z. Unlike existing acoustic tweezers, our JSAT system is able to control all six fundamental motions and achieve complex manipulation combined with controlled translational and rotational motions, thus facilitating comprehensive cell manipulation in a 3D space. In addition to these features, our system can control the force applied to an acoustically trapped cell to gradually deform the cell. This ability allows for the introduction of controllable mechanical perturbations to single cells for detailed characterization of cellular responses at different levels of mechanical perturbations.

Results

Mechanisms of JSAT

The JSAT system can exert and control both the acoustic radiation force and viscous torque applied on a cell to enable precise and controllable six fundamental motions (three translational and three rotational motions) manipulation of the cell. To enable this ability, our JSAT system leverages a unique array of interdigital transducers (IDTs) deposited on a $LiNbO_3$ substrate to generate and control both the SAW and acoustic streaming fields inside a polydimethylsiloxane (PDMS)-based microfluidic chamber. As illustrated by a device schematic in Fig. 1a (also see Supplementary Fig. S1), the entire array is composed of three (i.e., inner, middle, and outer) subarrays that have collections of 4, 4, and 8 IDTs (denoted as $\{IDT_i^{out}\}_4$, $\{IDT_j^{mid}\}_4$, and $\{IDT_k^{in}\}_4$, respectively) for generating SAWs at different frequencies. Such design is difficult to achieve using thickness-mode piezoelectric transducers (such as PZTs), as the bulk acoustic waves generated by a PZT are impeded by other PZTs placed in the wave propagation path. This limits the options of integrating multiple PZTs for achieving complex cell/particle manipulation functions. Conversely, SAWs generated by an IDT exhibit good transmissibility through regions with IDTs working at different frequencies, thereby allowing more options for designing complex IDT arrays. Supplementary Fig. S2 shows a photo of a fabricated JSAT device with an IDT array and a microfluidic chamber. The mechanisms for achieving multi-DoF manipulation of single cells using the three subarrays are presented below.

The outer subarray enables cell trapping by leveraging acoustic radiation force and controlling the trapped cell's three translational motions (i.e., u_x, u_y, and u_z) through phase and amplitude modulations of SAWs. This subarray has two orthogonal pairs of IDTs positioned along the x- and y-axes, respectively. When applying excitation signals to these IDTs at their resonance frequencies, a grid-like standing SAW field is formed within the microfluidic chamber. Consequently, a cell can be trapped by one of multiple Gor'kov potential wells due to the acoustic radiation force[79,80] applied to the cell. Moreover, the trapped cell can be precisely translated with a displacement of u_x (or u_y), by moving the Gor'kov potential well's position through phase modulation, i.e., changing the phase difference between the two IDTs along the x- (or y-) axis. In addition, the SAW energy leaked into the fluid domain in the PDMS chamber induces an out-of-plane acoustic radiation force, as illustrated in Fig. 1b (top right). The out-of-plane translation u_z of the acoustically trapped cell can be precisely controlled by adjusting the IDT excitation voltage, which regulates the force component responsible for the translation.

The middle subarray controls the trapped cell's rotational DoFs θ_x and θ_y by utilizing standing SAW-induced acoustic streaming vortices. The middle subarray's two IDTs positioned along the x-axis generate acoustic streaming vortices with non-zero angular momentums, enabling precise control of cell rotation θ_x, as shown in Fig. 1b (bottom left). Similarly, the two IDTs along the y-axis can generate vortices, enabling precise control of cell rotation θ_y, as illustrated in Fig. 1b (bottom middle). The operation frequencies of these middle subarray IDTs are higher than the frequencies of the outer subarray IDTs, so the diameter (~ 25 μm) of each streaming vortex is comparable to the cell size. The generated streaming vortices can apply a viscous torque to the cell, introducing angular momentum. Moreover, the cell angular velocities can be altered by adjusting the input voltages applied to the middle subarray.

https://doi.org/10.1038/s41467-024-52686-8

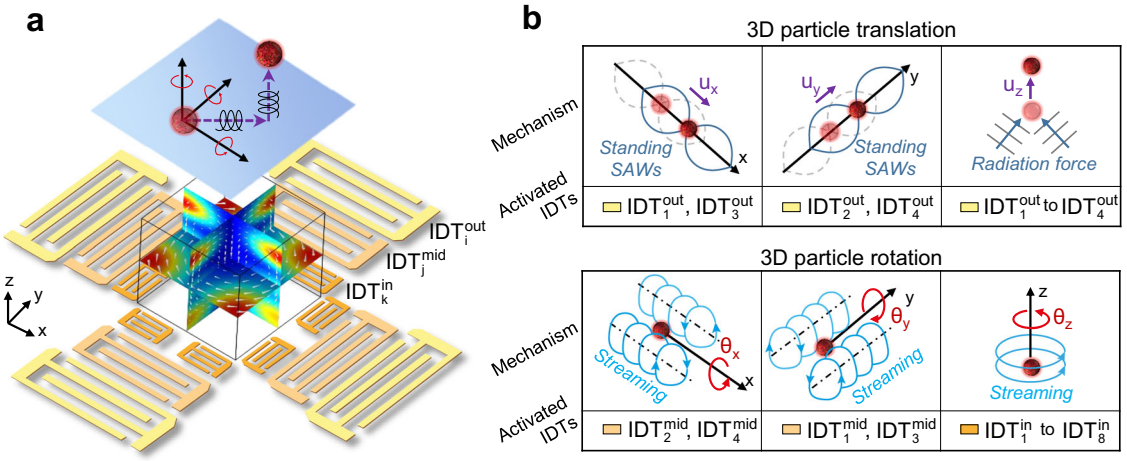

Fig. 1 | Schematics illustrating the mechanism of the JSAT for 6 fundamental single-cell manipulation. a A schematic of a JSAT chip composed of a $LiNbO_3$ substrate deposited with an array of IDTs and a PDMS-based microfluidic chamber. The IDTs are organized into outer ("out"), middle ("mid"), and inner ("in") segments, as indicated by superscripts, and are indexed by subscripts i, j, and k. The details of the IDT labels are given in Supplementary Fig. S1. This IDT array configuration generates controllable acoustic pressure fields and streaming patterns, allowing precise control of the multi-DoF motions of single cells in the microfluidic chamber. **b**, top Schematics illustrating the mechanisms of controlling 3D translations (u_x, u_y, and u_z) of an acoustically trapped cell. The in-plane translation u_x (or u_y) is achieved by shifting the pressure node position by changing the phase difference between input signals for IDT_1^{out} and IDT_3^{out} (or IDT_2^{out} and IDT_4^{out}). The out-of-plane translation u_z is achieved by adjusting the time of input voltages for IDT_1^{out} to IDT_4^{out}. **b**, bottom Schematics illustrating the mechanisms of controlling 3D rotations (θ_x, θ_y, and θ_z). To control the rotation θ_x (or θ_y) of an acoustically trapped cell, streaming vortices induced by standing SAWs generated from IDT_2^{mid} and IDT_4^{mid}(or IDT_1^{mid} and IDT_3^{mid}) are used. To control the cell rotation θ_z, a streaming vortex induced by traveling SAWs generated from IDTs of the inner subarray is adopted.

The inner subarray controls the trapped cell's rotation θ_z by manipulating the traveling SAW-induced acoustic streaming vortices. Here, the inner subarray's four IDTs with even subscripts (see Supplementary Fig. S1) are utilized to generate traveling SAWs whose energy beam directions are tangential to a circle. These traveling SAWs can induce an in-plane acoustic streaming vortex with a clockwise angular momentum, resulting in the ability to rotate a cell clockwise. On the other hand, the four IDTs with odd subscripts can be used to generate a counterclockwise acoustic streaming vortex to enable the counterclockwise rotation of a cell, as illustrated in Fig. 1b (bottom right). Moreover, by tuning the input voltages for these IDTs, the angular movement of the generated streaming vortex can be adjusted to control the angular velocity of the cell.

As presented above, by leveraging three subarrays of IDTs, our JSAT system can trap a cell and control the cell's six fundamental motions. Moreover, through the superposition of forces/torques generated by IDTs to control different DoFs, our JSAT system enables complex manipulation of a trapped cell, allowing for simultaneous translation and rotation. Furthermore, by slowly increasing the force applied on a cell, our device can gradually deform an acoustically trapped cell. We have performed simulations and experiments with key results reported below to achieve and validate these functions.

3D translation via JSAT

To trap a cell and control its 3D translational motion, the outer subarray leverages two orthogonal pairs of IDTs (see Fig. 2a) to generate SAWs with the same wavelength ($\lambda^{out} = 200\ \mu m$) in both the x- and y-directions. The interaction of SAWs generated from these four IDTs leads to a square grid-like distribution of pressure nodes (or antinodes) with the same period of $\lambda^{out}/2$ along the x- and y- directions. At each pressure node, the resulting Gor'kov potential well can trap a cell with a positive acoustic contrast factor[81]. Since cells typically have dimensions in tens of microns, the low frequencies used ensure the in-plane Stokes drag force resulting from acoustic streaming is negligible compared to the in-plane acoustic radiation force for trapping the cell. To achieve controllable in-plane translations u_x and u_y of a trapped cell, our system leverages the phased modulation approach, which tunes the phase differences φ_x and φ_y between excitation signals for the two IDTs along the x- and y-directions, respectively. As shown by the simulated acoustic energy fields, when phase differences change from $\boldsymbol{\varphi}$ (Fig. 2b, left) to $\boldsymbol{\varphi} + \Delta\boldsymbol{\varphi}$ (Fig. 2b, right), where $\boldsymbol{\varphi} = [\varphi_x, \varphi_y]$ and $\Delta\boldsymbol{\varphi} = [\Delta\varphi_x, \Delta\varphi_y]$, the potential well with the trapped cell can be shifted by a short translation vector $\boldsymbol{u} = [u_x, u_y, 0]$ with $u_x = \Delta\varphi_x\lambda^{out}/(4\pi)$ and $u_y = \Delta\varphi_y\lambda^{out}/(4\pi)$. Based on this mechanism, a long and complex translation path can be achieved by discretizing the path into a series of short translation vectors, calculating the required phase adjustments for these vectors, and sequentially applying the phase adjustments to IDT excitation signals. To execute this translation process automatically, the phase adjustments can be sequentially applied through two dual-channel function generators controlled by MATLAB code. To demonstrate this ability, we successfully guided an MCF7 cell's movement to depict the letters 'D', 'U', 'K', and 'E' (see Supplementary Movie 1). The actual cell trajectories (see Fig. 2c) were revealed by stacking the microscopic images captured during the dynamic cell translation process. As shown in Supplementary Fig. S3, the actual cell positions closely agree with the predicted positions using relations $u_x = \Delta\varphi_x\lambda^{out}/(4\pi)$ and $u_y = \Delta\varphi_y\lambda^{out}/(4\pi)$. As the phase modulation-based translational manipulation mechanism is known for its good predictability[2], we didn't perform any calibration before translating an MCF7 cell following complex trajectories.

To achieve controllable out-of-plane translation u_z of a trapped cell, our system leverages the amplitude modulation approach, which adjusts the excitation amplitudes of the outer subarray's four IDTs. The experimental results demonstrate that the position of an MCF7 cell can be shifted in the + z-direction through acoustic waves generated by the IDTs (see Fig. 2e and Supplementary Movie 2). To better elucidate the manipulation mechanism, finite element simulations were performed. As SAWs propagate in the $LiNbO_3$ substrate, their energy leaks into the fluid domain above the substrate, leading to an energy flux along the Rayleigh angle direction, as illustrated in Fig. 2d. Therefore, a cell within the vicinity is subjected to an out-of-plane acoustic radiation force component $F_{rad\_z}^{out}$, which points to the + z-direction acting as the levitation driving force, as predicted by simulation results in

https://doi.org/10.1038/s41467-024-52686-8

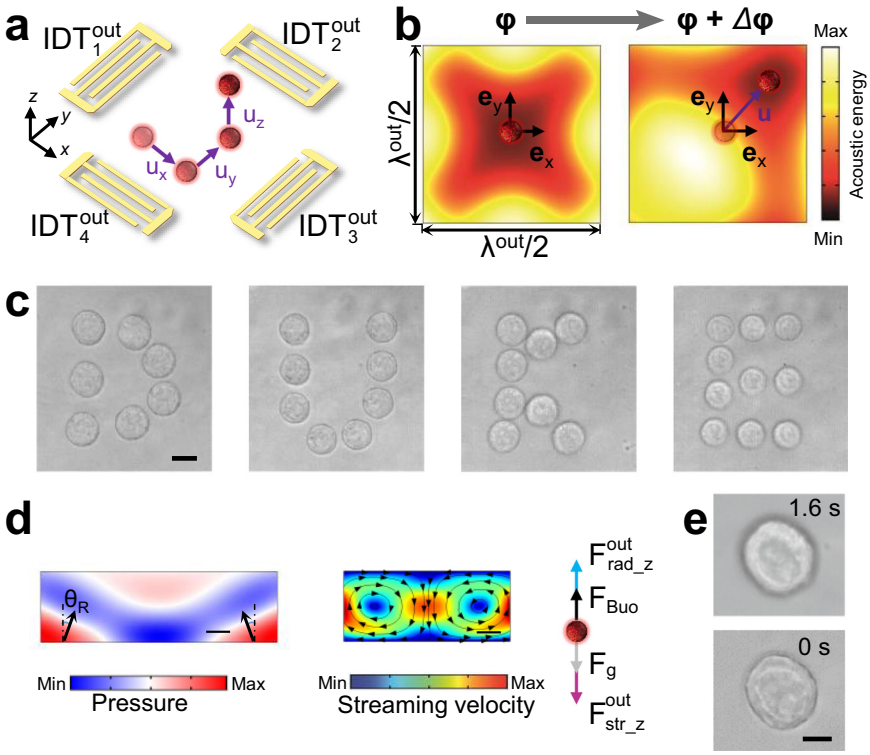

Fig. 2 | 3D translations of an acoustically trapped MCF7 cell. a Schematic illustrating the 3D translations of a cell using the outer subarray with IDT_1^{out} to IDT_4^{out}. **b** Numerical simulations of in-plane acoustic energy fields in an area with dimensions $\lambda^{out}/2 \times \lambda^{out}/2$, where λ^{out} is the wavelength of SAWs generated by IDT_1^{out} to IDT_4^{out}. When small changes $\Delta\boldsymbol{\varphi} = [\Delta\varphi_x, \Delta\varphi_y]$ are applied to phase differences $\boldsymbol{\varphi} = [\varphi_x, \varphi_y]$, a cell trapped in a potential well can be shifted by a displacement vector $\boldsymbol{u} = [u_x, u_y, 0]$. Here, φ_x (or φ_y) is the phase difference between excitation signals for IDT_1^{out} and IDT_3^{out} (or IDT_2^{out} and IDT_4^{out}). **c** Stacked microscopic images showing an MCF7 cell can be translated along complex paths by applying predetermined phase differences to IDT excitation signals. The cell trajectories depict four letters: "D", "U", "K", and "E". Scale bar, 10 µm. Each letter depiction was repeated three times, consistently yielding similar results. **d**, left Simulated acoustic pressure field in the fluid domain showing pressure waves induced by counter-propagating SAWs in the $LiNbO_3$ substrate. The pressure wave propagation direction has an angle θ_R (i.e., Rayleigh angle) with respect to the *z*-axis. The wave momentum in the + *z*-direction can generate an acoustic radiation force component $F_{rad\_z}^{out}$. **d**, middle Simulated acoustic streaming field induced by standing SAWs showing two counter-chirality streaming vortices at different sides of a pressure node. At the pressure node (i.e., the center of the simulation domain), the streaming flow is in the − z-direction, thus applying a downward drag force on a cell trapped at the pressure node. **d**, right Illustration of forces applied on a cell, implying that the cell's *z* position depends on the action of vertical force components, including the acoustic streaming-induced drag force $F_{str\_z}^{out}$, gravitational force F_g, acoustic radiation force $F_{rad\_z}^{out}$, and buoyancy force F_{Buo}. **e** Microscopic images validating the u_z translation of a cell. When activating the IDTs for 1.6 s, the microscopic image of an MCF7 cell becomes out of focus due to the cell's *z*-position change. The translation was repeated three times, consistently yielding similar results. Scale bar: 10 µm.

Supplementary Fig. S4. Additional theoretical investigation of the out-of-plane acoustic radiation force can be found in our previous article[82]. An acoustofluidic simulation was also performed to analyze the acoustic streaming-induced out-of-plane Stokes drag force. As shown in the simulation results (Supplementary Fig. S5 and Fig. 2d, middle), there is a downward acoustic streaming at the pressure node, thus inducing a − *z*-direction drag force that gradually diminishes from the microfluidic chamber's center to the bottom and top (see Supplementary Fig. S5). The out-of-plane translation u_z depends on the interplay of all the out-of-plane forces, including the position-dependent acoustic radiation and drag forces, the buoyancy force F_{Buo}, and the gravitational force F_g, as shown in Fig. 2d (right). Most cells, including MCF7 cells, have a density slightly higher than the culture medium (water with additives), so the *z*-directional manipulation can be controlled theoretically by applying a precise input power to match to account for the aforementioned out-of-plane forces. However, the control of out-of-plane translation cannot be as precise and stable as the control of in-plane translation due to the absence of a Gor'kov potential well-like trap. In addition, when the cell experiences other motions, especially rotational motions, they affect the out-of-plane translation. The out-of-plane translation precision is also affected by the two-dimensional imaging nature of our current microscope, as the translation is difficult to be quantitively monitored.

3D rotation via JSAT

To control an acoustically trapped cell's 3D rotational motion, our JSAT device leverages the middle and inner subarrays of IDTs to generate and control acoustic streaming vortices for applying and controlling viscous torques on the cell. The IDT_2^{mid} and IDT_4^{mid} of the middle subarray are for controlling the cell rotation θ_x using acoustic streaming, as illustrated in Fig. 3a. They generate standing SAWs with a wavelength λ^{mid} of 100 µm, further inducing tunnel-like streaming vortices with counter chiralities at different sides of each pressure node, as revealed by the results in Supplementary Fig. S6 and Supplementary Movie 3. Therefore, for a cell trapped at a pressure node, the two counter-chirality vortices both apply torques to the cell, and the competition between the two vortices determines the cell's angular motion. To better elucidate the cell manipulation mechanism, we performed numerical simulations with the excitation voltage V_2^{mid} for IDT_2^{mid} slightly higher than the voltage V_4^{mid} for IDT_4^{mid}. As shown in Supplementary Fig. S6, the streaming fields of vortices on different sides of a pressure node become slightly asymmetric. These asymmetric vortices can lead to a non-zero viscous torque applied on the cell, consequently inducing cell rotation. Moreover, our simulation results (Supplementary Fig. S6d, S6e) reveal that the tangential streaming velocities can lead to cell rotation in the + θ_x-direction being dominant. Furthermore, during the streaming-induced cell rotation,

https://doi.org/10.1038/s41467-024-52686-8

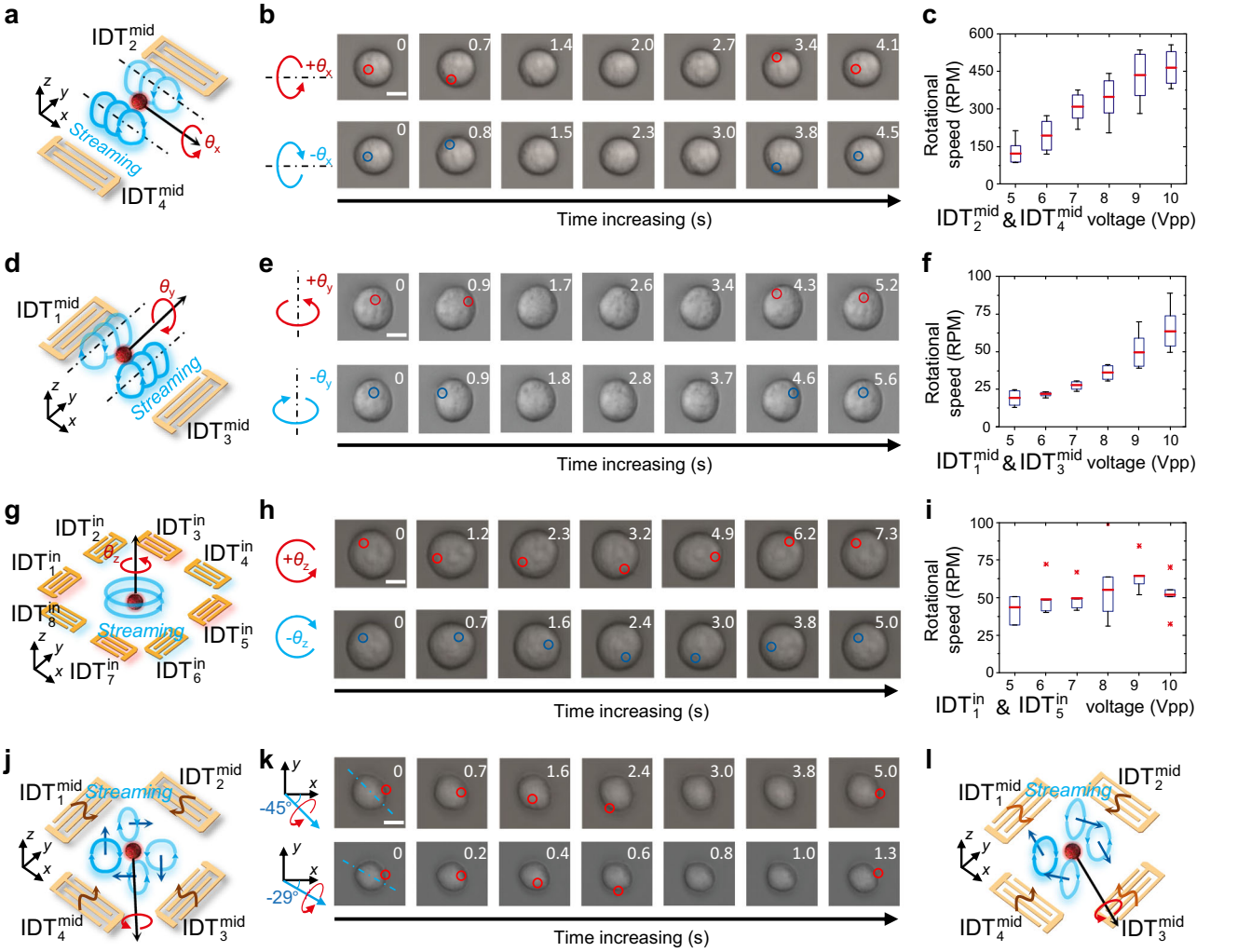

Fig. 3 | 3D rotations of an acoustically trapped MCF7 cell. a Schematic of a cell rotating in the θ_x-direction driven by acoustic streaming generated by IDT_2^{mid} and IDT_4^{mid}. **b** Sequential images showing an MCF7 cell rotated in the + θ_x-direction when $V_4^{mid}<V_2^{mid}$ (top row) and − θ_x-direction when $V_4^{mid}>V_2^{mid}$. Scale bar: 10 µm. **c** Analysis results of rotated cells (Doing N repeated tests with different cells: N = 4) showing the cell rotation speed in the + θ_x-direction gradually increases with the input voltage increase. **d** Schematic of a cell rotating in the θ_y-direction driven by acoustic streaming generated by IDT_1^{mid} and IDT_3^{mid}. **e** Sequential images showing an MCF7 cell spined in the + θ_y- (top row) and − θ_y- (bottom row) directions. Scale bar: 10 µm. **f** Analysis results of rotated cells (Doing N repeated tests with different cells: $N = 4$) showing the cell rotation speed in the + θ_y-direction gradually increases with the input voltage increase. **g** Schematic of a cell rotating in the θ_z-direction driven by acoustic streaming generated by IDT_1^{in} to IDT_8^{in} **h** Sequential images showing an MCF7 cell rotated in the + θ_z-direction when activating IDT_1^{in} and IDT_5^{in} as well as − θ_z-direction when activating IDT_2^{in} and IDT_6^{in}. Scale bar: 10 µm. (**i**) Analysis results of cell rotation speeds (Doing N repeated tests with different cells: $N \geq 3$) in the + θ_z-direction at different excitation voltages. **j** Schematic illustrating the mechanism to induce cell rotation carrying an angular momentum in − 45° in the *x*-*y* plane. **k** Sequential images showing an MCF7 cell rotated with respect to axes of − 45° (top) and − 29° (bottom) in the *x*-*y* plane. Scale bar: 10 µm. **l** Schematic illustrating the mechanism to induce cell rotation carrying an angular momentum in − 30° in the *x*-*y* plane. In (**c**, **f**, and **i**), each box plot displays statistical measures: the central red line indicates the average value, and the bottom and top of the box represent the 25th and 75th percentiles, respectively. Whiskers extend to the lowest datum within 1.5 times the interquartile range (IQR) from the 25 th percentile and the highest datum within 1.5 times the IQR from the 75 th percentile. Outliers are donated by asterisks.

the acoustic potential well generated by the standing SAWs can still effectively trap the cell, ensuring no translational motion or eccentricity. The experimental validation results (top of Fig. 3b and Supplementary Movie 3) show that an MCF7 cell could be successfully trapped and rotated in the + θ_x-direction when $V_4^{mid}<V_2^{mid}$, agreeing with the numerically predicted rotation direction. Therefore, we can reliably execute the rotational manipulation as planned. Similarly, under the condition of $V_4^{mid}>V_2^{mid}$, an acoustically trapped MCF7 cell exhibited rotation in the − θ_x-direction (Fig. 3b, bottom and Supplementary Movie 3). Note that the aforementioned rotation control approach is for a cell located near the center of the microfluidic chamber, as the SAWs emitted from a pair of IDTs travel to the center region with similar attenuation lengths. When the cell position is close to either IDT_2^{mid} or IDT_4^{mid}, asymmetric streaming vortices can still be generated at different sides of a pressure node even $V_2^{mid}=V_4^{mid}$, enabling cell rotation in the ± θ_x-directions.

To investigate the relationship between input voltage and cell rotation speed, we loaded an MCF7 cell at a distance of $\lambda^{mid}/2$ away from the center, followed by applying the same voltage to IDT_2^{mid} and IDT_4^{mid}. As depicted in Fig. 3c, the rotation speed exhibited a positive correlation with the input voltage and could reach values as high as ~ 450 RPM in the cell culture medium. Furthermore, the cell rotation revolution shows a nearly linear relationship with time (see Supplementary Fig. S7). These findings indicate that the cell's spinning rate remains relatively stable during the streaming generation period. In addition, by activating IDT_1^{mid} and IDT_3^{mid} to generating streaming vortices, we successfully induced the rotation of an MCF7 cell in the ±θ_y-directions (Fig. 3e and Supplementary Movie 4). The

corresponding relationship between input voltage and rotation speed is summarized in Fig. 3f.

For enabling cell rotation in the θ_z-direction, the inner subarray (Fig. 3g) is used. When signals at resonant frequencies are applied to the four IDTs with odd subscripts, the traveling SAW from each IDT produces a volume force that propels the fluid away from the IDT. Consequently, the combined effect of the four driving flows forms a counterclockwise streaming vortex. Note that when only activating IDT_1^{in} and IDT_5^{in}, a counterclockwise streaming vortex can still be generated, as proven by numerical and experimental results (Supplementary Fig. S8 and Supplementary Movie 5). Therefore, an MCF7 cell, driven by the viscous torque induced by the counterclockwise streaming vortex, can be rotated in the $+\theta_z$-direction (see Fig. 3h, top and Supplementary Movie 5). Similarly, the IDTs with even subscripts in the inner subarray can induce cell rotation in the $-\theta_z$-direction. Through experiments with IDT_2^{in} and IDT_6^{in} turned on, the results (Fig. 3h, bottom and Supplementary Movie 5) successfully confirm the induced cell rotation in the $-\theta_z$-direction. Furthermore, we experimentally investigated the relationship between input voltage and rotation speed. The findings reveal that the rotation speed exhibited an increasing trend as the input voltage increased (Fig. 3i). The slight spin rate drops at 10 Vpp could be induced by measurement error.

Tunable rotation via JSAT

Our device can steer the cell rotation axis by simultaneously activating the two orthogonal pairs of IDTs in the middle subarray for rotating a cell in the θ_x- and θ_y- directions (Fig. 3j). Supplementary Fig. S9a presents the numerical results of acoustic streaming when x- and y-axes standing SAWs have the same amplitude. In the vicinity of a pressure node, the results show four vortices with angular momentum vectors in −45°, 45°, 135°, and −135° directions, respectively. Similar to controlling the cell rotation in the θ_x-direction, the middle subarray can rotate a trapped cell in the same direction as any one of those four vortices by adjusting the voltages applied to the four IDTs or placing the cell off-center. For instance, an MCF7 cell trapped at $x = \lambda^{mid}/2$ and $y = \lambda^{mid}/2$ was successfully spun to carry an angular momentum in the direction of −45° (see Fig. 3k and Supplementary Movie 6), x- and y-axes SAWs had similar amplitudes. Moreover, by carefully changing the amplitude ratio between x- and y-axes SAWs, the axis of cell rotation can be gradually steered. For example, when the ratio is 0.57:1, the simulation (Supplementary Fig. S9b) predicts four vortices surrounding a pressure node carrying angular momentums in −30°, 30°, 150°, and −150°. The experimental results (bottom row of Fig. 4k and Supplementary Movie 6) show a rotating MCF7 cell with respect to an axis at −29°, close to the predicted direction of −30°. When the SAW amplitude ratio further changes to 0.3:1, numerical simulations in Supplementary Fig. S9c reveal the four vortices with angular momentums at −15°, 15°, 165°, and −165°. The experimental results (Supplementary Fig. S9d and Supplementary Movie 6) confirm that an MCF7 cell trapped at $x = \lambda^{mid}/2$ and $y = \lambda^{mid}/2$ can be rotated to carry an angular momentum in the direction of −15°, agreeing with the numerical prediction. Note that when adjusting input voltages for

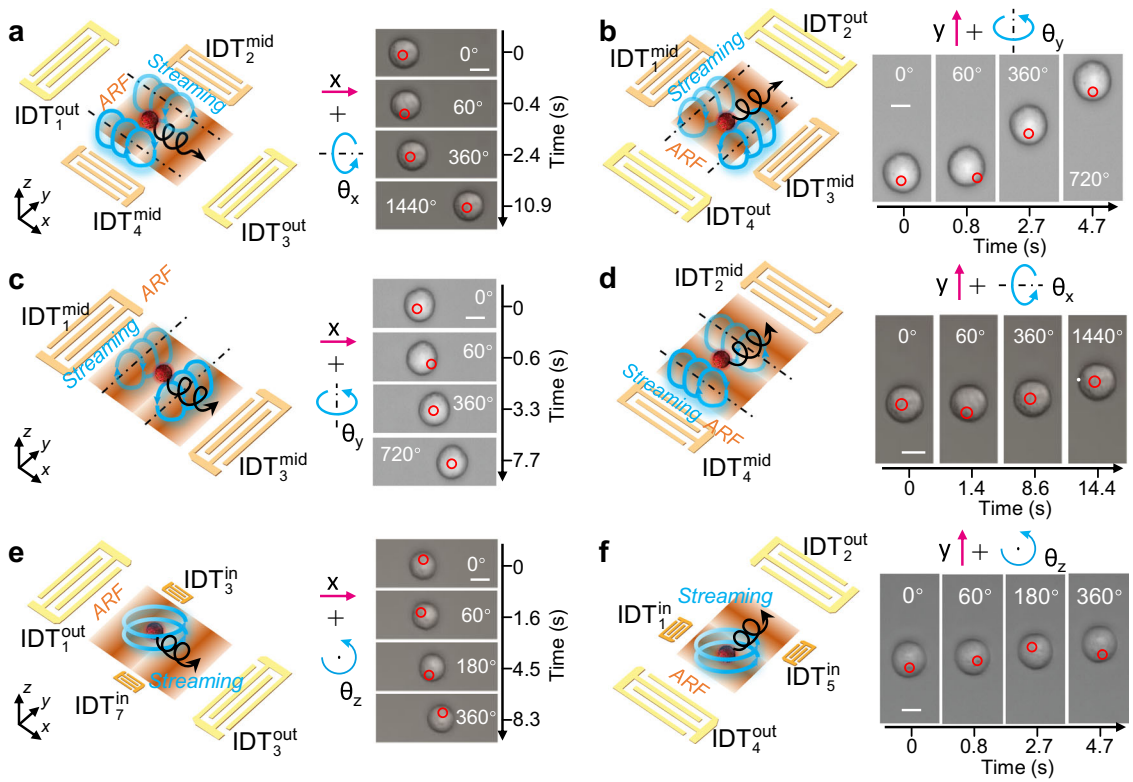

Fig. 4 | Simultaneous translation and rotation of an MCF7 cell via JSAT. a A schematic and experimental results for simultaneously translating a cell in the $+x$-direction using the x-axis standing SAWs generated by IDT_1^{out} and IDT_3^{out}, as well as rotating the cell in the $+\theta_x$-direction using streaming generated by IDT_2^{mid} and IDT_4^{mid}. **b** A schematic and experimental results for simultaneously translating a cell in the $+y$-direction using the y-axis standing SAWs generated by IDT_2^{out} and IDT_4^{out}, as well as rotating the cell in the $+\theta_y$-direction using streaming generated by IDT_1^{mid} and IDT_3^{mid}. **c** A schematic and experimental results for simultaneously translating a cell in the $+x$-direction using a potential well, as well as rotating the cell in the $+\theta_y$-direction using streaming generated by IDT_1^{mid} and IDT_3^{mid}. **d** A schematic and experimental results for simultaneously translating a cell in the $+y$-direction a potential well, as well as rotating the cell in the $+\theta_x$-direction using streaming generated by IDT_2^{mid} and IDT_4^{mid}. **e** A schematic and experimental results for simultaneously translating a cell in the $+x$-direction using x-axis standing SAWs generated by IDT_1^{out} and IDT_3^{out}, as well as rotating the cell in the $+\theta_z$-direction using streaming generated by IDT_3^{in} and IDT_7^{in}. **f** A schematic and experimental results for simultaneously translating a cell in the $+y$-direction using y-axis standing SAWs generated by IDT_2^{out} and IDT_4^{out}, as well as rotating the cell in the $+\theta_z$ direction using streaming generated by IDT_1^{in} and IDT_5^{in}. Scale bar: 10 μm.

IDTs, the different SAW generation efficiencies in the x- and y- directions of the used Y128-cut $LiNbO_3$ wafer must be considered.

Simultaneous translation and rotation via JSAT

A unique feature of our JSAT platform is its ability to perform simultaneous cell translation and rotation. To understand such compound motion, we conducted simulations and experiments involving different combinations of translation and rotation directions. Figure 4a (left) illustrates the mechanism to simultaneously translate a trapped cell in the x-direction and rotate the cell in the θ_x-direction. The translation is controlled by tuning the input phase difference between IDT_1^{out} and IDT_3^{out}, and the rotation is controlled by the streaming vortex generated by IDT_2^{mid} and IDT_4^{mid}. Supplementary Fig. S10 compares acoustic energy distributions of standing SAWs generated by one transducer pair {IDT_1^{out}, IDT_3^{out}} and two transducer pairs {IDT_1^{out}, IDT_3^{out}} and {IDT_2^{mid}, IDT_4^{mid}}. The x position with minimum energy is unchanged upon introducing the y-axis SAWs from {IDT_2^{mid}, IDT_4^{mid}}, meaning that the positional stability of a trapped cell is unaffected by the y-axis SAWs. On the other hand, we found that the x-axis standing SAW exhibits negligible impact on the generation of streaming vortices with angular momentum vectors in $\pm x$-directions. These simulation results support the simultaneous execution of cell translation and rotation and control these motions using transducer pairs {IDT_1^{out}, IDT_3^{out}} and {IDT_2^{mid}, IDT_4^{mid}}, respectively. For the proof-of-concept, we successfully utilized these two transducer pairs to achieve controlled translation in the x-direction and rotation in the θ_x-direction (Supplementary Movie 7 and Fig. 4a, right). As the x-axis standing SAW generated from {IDT_1^{out}, IDT_3^{out}} exhibits negligible impact on the streaming vortices generated by {IDT_2^{mid}, IDT_4^{mid}} and the two streaming vortex tunnels are parallel to the cell translation direction, our approach achieves continuous cell rotation during the translation process. Similarly, we manipulated an MCF7 cell to undergo both translation in the y-direction and rotation in the θ_y-direction (Supplementary Movie 7 and Fig. 4b, right) by using transducer pairs {IDT_2^{out} IDT_2^{out}, IDT_4^{out}} and {IDT_1^{mid}, IDT_3^{mid}}.

The mechanism to enable simultaneous cell translation in the x-direction and rotation in the θ_y-direction is illustrated in Fig. 4c (left). Here, the translation control is achieved by tuning the phase difference between inputs for IDT_1^{mid} and IDT_3^{mid}, and the rotation is enabled by streaming vortices generated by the x-axis standing SAWs. To demonstrate this approach, we performed an experiment with IDT_1^{mid} and IDT_3^{mid} turned it on. By gradually adjusting the phase difference, our results (Supplementary Movie 8 and Fig. 4c, right) show that the generated standing SAWs can translate an MCF7 cell in the x-direction while inducing acoustic streaming to spin the cell in the θ_y-directions. Although both acoustic radiation force and streaming are generated by the same IDTs, the translation u_x is controlled by the input phase difference, and the rotation θ_y is controlled by the input amplitude difference between the two IDTs. Hence, the involved translational and rotational motions could be independently controlled. Moreover, when translating a cell through phase modulation, the positions of two streaming vortex tunnels (illustrated in Fig. 4c) shift synchronously, thus ensuring continuous cell rotation during the translation process. By using the above mechanisms with IDT_2^{mid} and IDT_4^{mid}, we achieved simultaneous translation of an MCF7 in the y-direction and rotation in the θ_x-direction (Fig. 4d and Supplementary Movie 8).

The mechanism to achieve simultaneous cell translation in the x-direction and rotation in the θ_z-direction is illustrated in Fig. 4e (left). By tuning the phase difference between inputs for IDT_1^{out} and IDT_3^{out}, the pressure node position of an x-axis standing SAW can be adjusted to translate a trapped cell in the x-direction. On the other hand, the θ_z-direction cell rotation can be achieved using the streaming vortex induced by the traveling SAWs from IDT_3^{in} and IDT_7^{in}. By comparing the simulated acoustic energy fields (Supplementary Fig. S11) generated by one transducer pair {IDT_1^{out}, IDT_3^{out}} and two transducer pairs {IDT_1^{out}, IDT_3^{out}} and {IDT_3^{in}, IDT_7^{in}}, the acoustic energy field experiences small changes when considering the traveling SAWs from {IDT_3^{in}, IDT_7^{in}}. On the other hand, the simulated streaming field (Supplementary Fig. S11) shows a counterclockwise streaming vortex. These simulation results support the simultaneous control of the cell translation in the x-direction and the rotation in the θ_z-direction by leveraging transducer pairs {IDT_1^{out}, IDT_3^{out}} and {IDT_3^{in}, IDT_7^{in}}, respectively. Our experiment successfully achieved simultaneous translation of an MCF7 cell in the x-direction and rotation in the θ_z-direction (Supplementary Movie 9 and Fig. 4e, right). Similarly, we achieved concurrent translation and rotation of an MCF7 cell in the y-and θ_z-directions (Supplementary Movie 9 and Fig. 4f, right) by using transducer pairs {IDT_2^{out}, IDT_4^{out}} and {IDT_1^{in}, IDT_5^{in}}.

Deforming single cells via JSAT

Our JSAT platform can locally deform single cells and control cell motion. As illustrated in Fig. 5a, when an acoustically trapped cell is positioned within a high angular momentum region of streaming vortices induced by standing SAWs generated by {IDT_2^{mid}, IDT_4^{mid}}, the streaming velocity in the cell's viscous boundary layer drops rapidly to the same value as the cell's surface velocity, thereby subjecting the cell to a large shear stress. Notably, the cell's surface velocity and shear stress exhibit a decreasing trend from the equator to the poles, prompting cell elongation along the axis of rotation (i.e., x-axis). The acoustic radiation force induced by y-axis standing SAWs also contributes to cell elongation.

To experimentally deform an MCF7 cell, we applied 10 Vpp excitation signals to IDT_2^{mid} and IDT_4^{mid}. The obtained time-sequential images (Fig. 5b) and Supplementary Movie 10 clearly show the dynamic process of gradually deforming a trapped cell over time. We also conducted a quantitative analysis by evaluating the gradual cell deformation over time and investigating the effect of the IDT excitation voltage on cell deformation. At 6 Vpp, the shape of an MCF7 cell remains almost unchanged throughout the 100-second observation period (see Fig. 5c). At a higher voltage of 8 Vpp, the cell deformation data exhibits a nearly linear trend with time. When the input voltage was further increased to 10 Vpp, the cell deformation initially experienced a quick increase, followed by a slight decrease, and then converged to a relatively stable value. These findings indicate that the time-dependent cell deformation processes demonstrate distinct trends under different IDT excitation voltages, highlighting our JSAT device's ability to controllably deform acoustically trapped cells by tuning the generated SAWs and streaming.

Discussion

In this study, we successfully developed and demonstrated a JSAT platform that is capable of controlling the six fundamental motions of single cells, including three translational (i.e., u_x, u_y, and u_z) and three rotational (i.e., θ_x, θ_y, and θ_z) components. Our unique IDT array, composed of an outer, middle, and inner subarray, enables this ability. The in-plane translations (u_x and u_y) of a cell trapped in a Gor'kov potential well are achieved by shifting the potential well's position and tuning input signal phases for the outer subarray. By adjusting the input signal voltages for the outer subarray, our JSAT platform allows for controlling the out-of-plane translation (u_z), i.e., controlling a cell's z position with acoustic radiation, buoyancy, drag, and gravitational forces. The controllable rotations (θ_x and θ_y) of an acoustically trapped cell are accomplished based on acoustic streaming vortices induced by high-frequency standing SAWs from the middle subarray, and the rotation θ_z is achieved by using acoustic streaming vortices generated by multiple traveling SAWs, whose energy beam directions are all tangential to a circle.

With the aforementioned features, such as achieving the six fundamental motions of single cells and locally deforming a cell, our JSAT platform represents a significant advancement compared to previous

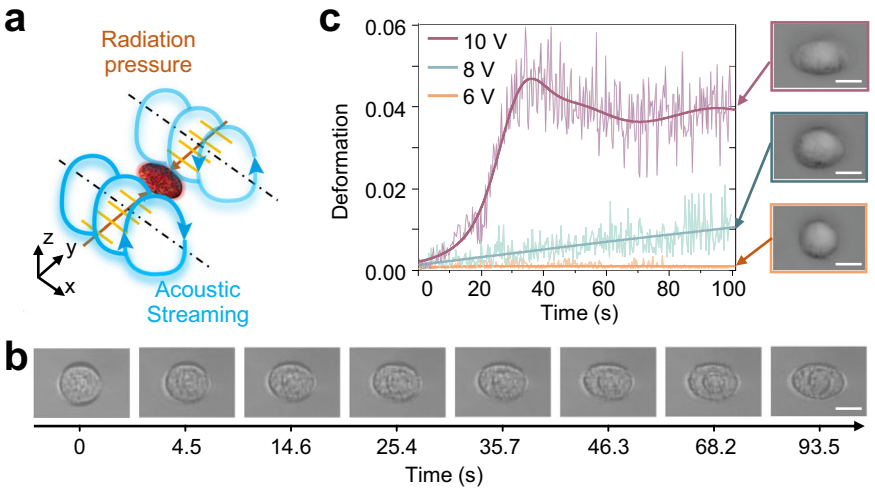

Fig. 5 | Controlled deformation of an acoustically trapped MCF7 cell via JSAT. **a** Schematic illustrating the mechanism of deforming an acoustically trapped cell. A cell trapped by a potential well of *y*-axis standing SAWs generated by IDT_2^{out} and IDT_4^{out} is subjected to both acoustic radiation and streaming vortex-induced shear forces, leading to cell deformation, *e.g.*, elongation along the axis of cell rotation. **b** Sequential images showing the gradual deformation of an MCF7 cell from a spherical shape to an ellipsoidal shape after applying standing SAWs. As the cell is acoustically trapped at a fixed position, our method allows for quantitatively examining the cell deformation. The experiment was repeated four times with different cells. **c** Deformation histories of an MCF7 cell. When using different input voltages for the transducer pair $\{IDT_2^{out}, IDT_4^{out}\}$, the deformation histories show diverse trends. The inset images are for cases with different input voltages, showing the shapes of an MCF7 cell after 100 s of acoustic waves. The experiment was repeated three times with different cells. Scale bar: 10 µm.

technologies, such as optical, magnetic, and acoustic tweezers. Our experiments successfully validated the ability to independently control the multi-DoF motions of an acoustically trapped cell, while none of the previously developed tweezers could provide this ability. Moreover, our experiments demonstrated the ability to realize complex combined motions, such as u_x and θ_x, u_x and θ_z, u_y and θ_z, etc., while previous tweezers could not perform these complex manipulations. Furthermore, our JSAT platform can gradually deform an acoustically trapped cell without directly touching the cell by controlling the applied shear force induced by streaming and acoustic radiation force from standing SAWs. Recording the dynamic cell deformation process makes it possible to characterize cell mechanical properties[83]. Therefore, contactless tweezers that can gradually deform a cell hold significant potential for cell phenotyping, disease diagnosis, and drug testing applications. Beyond the experiments conducted in this study, we will further test the ability to simultaneously deform multiple cells trapped in an array of potential wells. We also plan to introduce a feedback control loop that integrates live imaging, real-time decision-making, and programmable input signal modulation to enable platform automation. In addition, beyond manipulating cells, we expect that our tweezing mechanisms can be used for manipulating other bioparticles, such as embryos, bacteria, and extracellular vesicles, and these manipulations will be tested in our future studies. In the long run, we anticipate that the JSAT platform can become a widely used tool facilitating various applications such as 3D cell imaging, single-cell analysis, tissue engineering, disease diagnostics, and mechanobiology.

Methods

Device fabrication

A schematic and a photo of the fabricated JSAT device are shown in Supplementary Figs. S1 and S2, respectively. The JSAT device is composed of a PDMS microfluidic chamber and an array of IDTs on a Y128-cut $LiNbO_3$ wafer (500 mm thick). To fabricate IDTs, we transferred the designed electrode patterns to a wafer by standard photolithography[84]. Then, we conducted e-beam evaporation of 10 nm Cr and then 100 nm Au. After a lift-off process, we obtained a wafer with an IDT array composed of outer, middle, and inner subarrays, whose electrode widths were 50 µm, 25 µm, and 10 µm, respectively. On the other hand, the PDMS micro-chamber was fabricated by using standard soft-lithography and mold-replica steps. First, a 60 µm layer of photoresist (SU-8 50, KAYAKU) was coated on a 4-inch silicon wafer, followed by soft lithography and application of an SU-8 Developer (KAYAKU). Then, PDMS was poured over the SU-8 mold, degassed, and cured at 65 °C for 1 h. The cured PDMS was peeled off the silicon wafer and cut into the desired small-size blocks containing microfluidic chambers. The inlet and outlet of a microfluidic chamber were created with a puncher. The PDMS chamber and the SAW substrate with IDTs were surface treated by oxygen plasma for 5 mins (Plasma Cleaner Atto, Diener Electronic) and then bonded, followed by a heat treatment at 65 °C for 24 h.

Particle and cell sample preparation

Polystyrene particles (PSF-200NM, Magsphere) were suspended in deionized water to a concentration of ~1×10^6 cells/mL. MCF7 cells (ATCC) were cultured in DMEM (Gibco, Life Technologies), which contains 10% fetal bovine serum (Gibco, Life Technologies) and 1% penicillin-streptomycin (Mediatech) in an incubator (Heracell Vios 160i CO_2 incubator, Thermo Scientific) with a temperature of 37 °C and a CO_2 level of 5%. Before each experiment, cells were detached from the culture dish with trypsin-EDTA (Gibco, Life Technology) and resuspended in DMEM to a concentration of ~1×10^6 cells/mL.

Device operation

To perform cell manipulation experiments using our fabricated JSAT device, the device was mounted on the sample stage of an inverted optical microscope (TE2000U, Nikon). MCF7 cells suspended in DMEM were injected into the microfluidic chamber using a 1-mL syringe (309659, Becton Dickinson). To generate SAWs for applying acoustic radiation and viscous shear forces on cells, the input signals were generated by two dual-channel arbitrary function generators (AFG3102C, Tektronix) and then directly sent to IDTs. Note that the function generators were controlled by a MATLAB program to achieve automatic manipulation of acoustic and flow fields, along with the desired translation and rotation of an acoustically trapped MCF7 cell in the microfluidic chamber. To translate a cell along the desired complex paths, the frequencies and voltages for the IDTs remain constant, while shifts are made to the input phases. The phase shifts are automatically performed using customized MATLAB codes, having key features

including adjusting the phases, frequencies, and amplitudes of multiple signal channels, as well as gradually changing the phases following predetermined sequences of phases for achieving step-by-step translation of a cell. Images and videos were taken by a charge-coupled device camera (CoolSNAP HQ2, Photometrics). The videos for cell rotation speed measurement were recorded by a high-speed camera (Fastcam SA4, Photron).

Numerical simulations

The details of numerical simulation methods were provided in Supplementary Notes 1 and 2.

Cell deformation measurement

To evaluate cell deformation from an acquired microscopic image, we used feature and edge detection codes in Matlab to get the cell shape from the image. Then, the cell's projected area A and perimeter l were extracted from the identified cell shape. By further using a relation $1-2\sqrt{\pi A}/l$, the cell deformation induced by our JSAT platform was elevated[85]. In addition, we measured the SAW device's temperature, as well as the post-treatment cell viability. Their detailed procedures and results are in Supplementary Note 3 and Supplementary Figs. 13–15.

Reporting summary

Further information on research design is available in the Nature Portfolio Reporting Summary linked to this article.

Data availability

The authors declare that all data and code supporting the findings of this study are available within the article and the supplementary materials. Further information is available from the corresponding author upon request.

References

1. Berthelot, J. et al. Three-dimensional manipulation with scanning near-field optical nanotweezers. *Nat. Nanotechnol.* **9**, 295–299 (2014).
2. Guo, F. et al. Three-dimensional manipulation of single cells using surface acoustic waves. *Proc. Natl. Acad. Sci. USA* **113**, 1522–1527 (2016).
3. Huang, L., Zhao, P. & Wang, W. 3D cell electrorotation and imaging for measuring multiple cellular biophysical properties. *Lab Chip* **18**, 2359–2368 (2018).
4. Urbanska, M. et al. A comparison of microfluidic methods for high-throughput cell deformability measurements. *Nat. Methods* **17**, 587–593 (2020).
5. Wu, P.-H. et al. A comparison of methods to assess cell mechanical properties. *Nat. Methods* **15**, 491–498 (2018).
6. Ahmed, D. et al. Rotational manipulation of single cells and organisms using acoustic waves. *Nat. Commun.* **7**, 11085 (2016).
7. Chen, C. et al. Acoustofluidic rotational tweezing enables high-speed contactless morphological phenotyping of zebrafish larvae. *Nat. Commun.* **12**, 1118 (2021).
8. Maloney, J. M. et al. Mesenchymal stem cell mechanics from the attached to the suspended state. *Biophys. J.* **99**, 2479–2487 (2010).
9. Lautenschläger, F. et al. The regulatory role of cell mechanics for migration of differentiating myeloid cells. *Proc. Natl. Acad. Sci. USA* **106**, 15696 (2009).
10. Nyberg, K. D. et al. Quantitative deformability cytometry: Rapid, calibrated measurements of cell mechanical properties. *Biophys. J.* **113**, 1574–1584 (2017).
11. Di Carlo, D. A mechanical biomarker of cell state in medicine. *J. Lab. Autom.* **17**, 32–42 (2012).
12. Fregin, B. et al. High-throughput single-cell rheology in complex samples by dynamic real-time deformability cytometry. *Nat. Commun.* **10**, 415 (2019).
13. Guck, J. et al. The optical stretcher: A novel laser tool to micromanipulate cells. *Biophys. J.* **81**, 767–784 (2001).
14. Rosendahl, P. et al. Real-time fluorescence and deformability cytometry. *Nat. Methods* **15**, 355–358 (2018).
15. Xie, Y. et al. Probing cell deformability via acoustically actuated bubbles. *Small* **12**, 902–910 (2016).
16. Nematbakhsh, Y. & Lim, C. T. Cell biomechanics and its applications in human disease diagnosis. *Acta Mech. Sin.* **31**, 268–273 (2015).
17. Grier, D. G. A revolution in optical manipulation. *Nature* **424**, 810–816 (2003).
18. Yang, A. H. J. et al. Optical manipulation of nanoparticles and biomolecules in sub-wavelength slot waveguides. *Nature* **457**, 71–75 (2009).
19. Juan, M. L., Righini, M. & Quidant, R. Plasmon nano-optical tweezers. *Nat. Photon.* **5**, 349–356 (2011).
20. Juan, M. L., Gordon, R., Pang, Y., Eftekhari, F. & Quidant, R. Self-induced back-action optical trapping of dielectric nanoparticles. *Nat. Phys.* **5**, 915–919 (2009).
21. Wu, M. C. Optoelectronic tweezers. *Nat. Photon.* **5**, 322–324 (2011).
22. De Vlaminck, I. & Dekker, C. Recent advances in magnetic tweezers. *Annu. Rev. Biophys.* **41**, 453–472 (2012).
23. Trick, A. Y. et al. Filtration-assisted magnetofluidic cartridge platform for HIV RNA detection from blood. *Lab Chip* **22**, 945–953 (2022).
24. Alghane, M. et al. Streaming phenomena in microdroplets induced by Rayleigh surface acoustic wave. *J. Appl. Phys.* **109**, 114901 (2011).
25. Baudoin, M. et al. Folding a focalized acoustical vortex on a flat holographic transducer: Miniaturized selective acoustical tweezers. *Sci. Adv.* **5**, eaav1967 (2019).
26. Bernassau, A. L., MacPherson, P. G. A., Beeley, J., Drinkwater, B. W. & Cumming, D. R. S. Patterning of microspheres and microbubbles in an acoustic tweezers. *Biomed. Microdevices* **15**, 289–297 (2013).
27. Collins, D. J. et al. Acoustic tweezers via sub–time-of-flight regime surface acoustic waves. *Sci. Adv.* **2**, e1600089 (2016).
28. Delsing, P. et al. The 2019 surface acoustic waves roadmap. *J. Phys. D* **52**, 353001 (2019).
29. Dholakia, K., Drinkwater, B. W. & Ritsch-Marte, M. Comparing acoustic and optical forces for biomedical research. *Nat. Rev. Phys.* **2**, 480–491 (2020).
30. Shen, L. et al. Acousto-dielectric tweezers for size-insensitive manipulation and biophysical characterization of single cells. *Biosens. Bioelectron.* **224**, 115061 (2023).
31. Yafouz, B., Kadri, N. A. & Ibrahim, F. Dielectrophoretic manipulation and separation of microparticles using microarray dot electrodes. *Sensors* **14**, 6356–6369 (2014).
32. Pethig, R. Dielectrophoresis: Status of the theory, technology, and applications. *Biomicrofluidics* **4**, 022811 (2010).
33. Kim, D., Sonker, M. & Ros, A. Dielectrophoresis: From molecular to micrometer-scale analytes. *Anal. Chem.* **91**, 277–295 (2019).
34. Tanase, M., Biais, N., & Sheetz, M. Magnetic tweezers in cell biology. *Methods Cell Biol.* **83**, 473–493 (2007).
35. Gossett, D. R. et al. Hydrodynamic stretching of single cells for large population mechanical phenotyping. *Proc. Natl. Acad. Sci. USA* **109**, 7630–7635 (2012).
36. Wiklund, M. Acoustofluidics 12: Biocompatibility and cell viability in microfluidic acoustic resonators. *Lab Chip* **12**, 2018–2028 (2012).
37. Tao, R. et al. Bimorph material/structure designs for high sensitivity flexible surface acoustic wave temperature sensors. *Sci. Rep.* **8**, 9052 (2018).
38. Shpak, O. et al. Acoustic droplet vaporization is initiated by superharmonic focusing. *Proc. Natl. Acad. Sci. USA* **111**, 1697 (2014).
39. Melde, K., Mark, A. G., Qiu, T. & Fischer, P. Holograms for acoustics. *Nature* **537**, 518–522 (2016).

40. Laurell, T., Petersson, F. & Nilsson, A. Chip integrated strategies for acoustic separation and manipulation of cells and particles. *Chem. Soc. Rev.* **36**, 492–506 (2007).
41. Kooiman, K., Vos, H. J., Versluis, M. & de Jong, N. Acoustic behavior of microbubbles and implications for drug delivery. *Adv. Drug Del. Rev.* **72**, 28–48 (2014).
42. Friend, J. & Yeo, L. Y. Microscale acoustofluidics: Microfluidics driven via acoustics and ultrasonics. *Rev. Mod. Phys.* **83**, 647–704 (2011).
43. Gu, J. & Jing, Y. Modeling of wave propagation for medical ultrasound: a review. *IEEE Trans. Ultrason Ferroelectr. Freq. Control* **62**, 1979–1992 (2015).
44. Ding, X. et al. Cell separation using tilted-angle standing surface acoustic waves. *Proc. Natl. Acad. Sci. USA* **111**, 12992–12997 (2014).
45. Li, P. et al. Acoustic separation of circulating tumor cells. *Proc. Natl. Acad. Sci. USA* **112**, 4970 (2015).
46. Nam, J., Lim, H., Kim, C., Yoon Kang, J. & Shin, S. Density-dependent separation of encapsulated cells in a microfluidic channel by using a standing surface acoustic wave. *Biomicrofluidics* **6**, 024120 (2012).
47. Bruus, H. et al. Forthcoming Lab on a Chip tutorial series on acoustofluidics: Acoustofluidics—exploiting ultrasonic standing wave forces and acoustic streaming in microfluidic systems for cell and particle manipulation. *Lab Chip* **11**, 3579–3580 (2011).
48. Rufo, J., Cai, F., Friend, J., Wiklund, M. & Huang, T. J. Acoustofluidics for biomedical applications. *Nat. Rev. Methods Prim.* **2**, 30 (2022).
49. Zhang, P., Bachman, H., Ozcelik, A. & Huang, T. J. Acoustic Microfluidics. *Annu. Rev. Anal. Chem.* **13**, 17–43 (2020).
50. Habibi, R. et al. Exosome trapping and enrichment using a sound wave activated nano-sieve (SWANS). *Lab Chip* **20**, 3633–3643 (2020).
51. Rufo, J., Zhang, P., Zhong, R., Lee, L. P. & Huang, T. J. A sound approach to advancing healthcare systems: the future of biomedical acoustics. *Nat. Commun.* **13**, 3459 (2022).
52. Gu, Y. et al. Acoustofluidic centrifuge for nanoparticle enrichment and separation. *Sci. Adv.* **7**, eabc0467 (2021).
53. Ding, X. et al. Tunable patterning of microparticles and cells using standing surface acoustic waves. *Lab Chip* **12**, 2491–2497 (2012).
54. Collins, D. J. et al. Two-dimensional single-cell patterning with one cell per well driven by surface acoustic waves. *Nat. Commun.* **6**, 8686 (2015).
55. Yang, S. et al. Acoustic tweezers for high-throughput single-cell analysis. *Nat. Protoc.* **18**, 2441–2458 (2023).
56. Hao, N. et al. Acoustofluidics-assisted fluorescence-SERS bimodal biosensors. *Small* **16**, 2005179 (2020).
57. Hao, N. et al. Acoustofluidic multimodal diagnostic system for Alzheimer's disease. *Biosens. Bioelectron.* **196**, 113730 (2022).
58. Lu, H. et al. Rapid additive-free bacteria lysis using traveling surface acoustic waves in microfluidic channels. *Lab Chip* **19**, 4064–4070 (2019).
59. Chen, Z. et al. Acoustofluidic micromixers: From rational design to lab-on-a-chip applications. *Appl. Mater. Today* **26**, 101356 (2022).
60. Reboud, J. et al. Shaping acoustic fields as a toolset for microfluidic manipulations in diagnostic technologies. *Proc. Natl. Acad. Sci. USA* **109**, 15162–15167 (2012).
61. Ren, T., Steiger, W., Chen, P., Ovsianikov, A. & Demirci, U. Enhancing cell packing in buckyballs by acoustofluidic activation. *Biofabrication* **12**, 025033 (2020).
62. Wang, W. et al. Acoustic propulsion of nanorod motors inside living cells. *Angew. Chem. Int. Ed.* **53**, 3201–3204 (2014).
63. Liang, S. & Chaohui, W. Acoustic radiation force on a compressible cylinder in the standing surface acoustic wave (SSAW). *J. Appl. Phys.* **123**, 044504 (2018).
64. Liang, S. & Chaohui, W. Revised model for the radiation force exerted by standing surface acoustic waves on a rigid cylinder. *Phys. Rev. E* **97**, 033103 (2018).
65. Liang, S., Chaohui, W. & Qiao, H. The radiation force on a rigid sphere in standing surface acoustic waves. *J. Appl. Phys.* **124**, 104503 (2018).
66. Yang, S. et al. Harmonic acoustics for dynamic and selective particle manipulation. *Nat. Mater.* **21**, 540–546 (2022).
67. He, Y. et al. Acoustofluidic interfaces for the mechanobiological secretome of MSCs. *Nat. Commun.* **14**, 7639 (2023).
68. Bruus, H., Winckelmann, B. G., Bach, J. S., & Skov, N. R. 3D modeling of acoustofluidics in a liquid-filled cavity including streaming, viscous boundary layers, surrounding solids, and a piezoelectric transducer. AIMS *Math.* **4**, 99–111 (2019).
69. Barnkob, R. et al. Acoustically driven fluid and particle motion in confined and leaky systems. *Phys. Rev. Appl.* **9**, 014027 (2018).
70. Garg, N. et al. Rapid immunodiagnostics of multiple viral infections in an acoustic microstreaming device with serum and saliva samples. *Lab Chip* **19**, 1524–1533 (2019).
71. Busse, F. H. & Wang, T. G. Torque generated by orthogonal acoustic waves–Theory. *Acoust. Soc. Am. J.* **69**, 1634–1638 (1981).
72. Marzo, A. & Drinkwater, B. W. Holographic acoustic tweezers. *Proc. Natl. Acad. Sci. USA* **116**, 84 (2019).
73. Mishra, P., Hill, M. & Glynne-Jones, P. Deformation of red blood cells using acoustic radiation forces. *Biomicrofluidics* **8**, 034109 (2014).
74. Link, A. & Franke, T. Acoustic erythrocytometer for mechanically probing cell viscoelasticity. *Lab Chip* **20**, 1991–1998 (2020).
75. Silva, G. T. et al. Acoustic deformation for the extraction of mechanical properties of lipid vesicle populations. *Phys. Rev. E* **99**, 063002 (2019).
76. Liu, Y. & Xin, F. Deformation dynamics of spherical red blood cells in viscous fluid driven by ultrasound. *Phys. Fluids* **35**, 012011 (2023).
77. Ni, Z. et al. Modelling of SAW-PDMS acoustofluidics: physical fields and particle motions influenced by different descriptions of the PDMS domain. *Lab Chip* **19**, 2728–2740 (2019).
78. Destgeer, G. & Sung, H. J. Recent advances in microfluidic actuation and micro-object manipulation via surface acoustic waves. *Lab Chip* **15**, 2722–2738 (2015).
79. Marston, P. L. & Zhang, L. Radiation torques and forces in scattering from spheres and acoustical analogues. In *Advances in Imaging* (Optica Publishing Group, 2009).
80. Settnes, M. & Bruus, H. Forces acting on a small particle in an acoustical field in a viscous fluid. *Phys. Rev. E* **85**, 016327 (2012).
81. Augustsson, P., Karlsen, J. T., Su, H.-W., Bruus, H. & Voldman, J. Iso-acoustic focusing of cells for size-insensitive acousto-mechanical phenotyping. *Nat. Commun.* **7**, 11556 (2016).
82. Liang, S., Chaohui, W. & Qiao, H. Force on a compressible sphere and the resonance of a bubble in standing surface acoustic waves. *Phys. Rev. E* **98**, 043108 (2018).
83. Suresh, S. Biomechanics and biophysics of cancer cells. *Acta Mater.* **55**, 3989–4014 (2007).
84. Mei, J., Zhang, N., & Friend, J. Fabrication of surface acoustic wave devices on lithium niobate. *J. Vis. Exp.* https://doi.org/10.3791/61013 (2020).
85. Otto, O. et al. Real-time deformability cytometry: on-the-fly cell mechanical phenotyping. *Nat. Methods* **12**, 199–202 (2015).

Acknowledgements

We acknowledge the support from the National Science Foundation (CMMI-2104526 (Z.T.) and CMMI-2243771 (Z.T.)), the National Science Foundation Graduate Research Fellowship Program (2139754 (J.R.)), and the National Institutes of Health (R01GM144417 (Z.T.)).

Author contributions

L.S. conceived the idea. L.S. developed the models for simulations. L.S. designed, fabricated, and characterized JSAT devices. K.Y. and J.Z. fabricated the JSAT devices. L.S., N.H., Z.P., J.X., and C.C. conducted the experiments. L.S. analyzed the data. L.S., Z.T., J.R., N.U., and T.J.H. wrote the paper. T.J.H. and Z.T. supervised the study.

Competing interests

T.J.H. has co-founded a start-up company, Ascent Bio-Nano Technologies Inc., to commercialize technologies involving acoustofluidics and acoustic tweezers. All other authors declare no competing interests.

Additional information

Supplementary information The online version contains supplementary material available at https://doi.org/10.1038/s41467-024-52686-8.

Correspondence and requests for materials should be addressed to Zhenhua Tian or Tony Jun Huang.

Peer review information *Nature Communications* thanks Per Augustsson, and the other anonymous reviewer(s) for their contribution to the peer review of this work. A peer review file is available.